A stochastic geometrical 3D model for time evolution simulation of microstructures in SOC-electrodes

Léo Théodon, Jérôme Laurencin, Maxime Hubert, Peter Cloetens, Johan Debayle

A stochastic geometrical 3D model for time evolution simulation of microstructures in SOC-electrodes

L. Théodon[a,*], J. Laurencin[b], M. Hubert[b], P. Cloetens[c], J. Debayle[a]

[a] *MINES Saint-Etienne, CNRS, UMR 5307 LGF, Centre SPIN, Saint-Etienne, France.*
[b] *Université-Grenoble Alpes, CEA/LITEN, Grenoble, France.*
[c] *European Synchrotron Radiation Facility, Grenoble, France.*

Abstract

An original 3D stochastic geometrical model has been developed to simulate the microstructural evolution of porous solid-oxide cell electrodes made of yttria-stabilized zirconia and nickel. The microstructural change induced by Ni agglomeration has been more specifically simulated. The model is based on random sets and algorithms for solving the linear assignment problem related to the time evolution of one component in the microstructure. The possibility to generate realistic 3D microstructures with the model has been verified by comparing the geometrical characteristics of synthetic microstructures with those extracted from real electrode reconstructions. The ability of the Stochastic Time Evolution Microstructure (STEM) model to generate microstructures with evolving characteristics has been then illustrated and compared to real data obtained on aged electrodes. The error on most of the geometrical characteristics are in general lower than 10%, except in some particular cases, such as the microstructure factor. All the results have then been discussed and suggestions have been proposed for improving the model.

Keywords: 3D microstructure model, Nickel–YSZ electrode, Solid oxide fuel cell, stochastic geometry

1. Introduction

In a context of climate change and increasing scarcity of fossil fuels, the Solid Oxide Cells (SOCs) technology has attracted considerable attention in the recent years. Indeed, this high temperature electrochemical device could be used to match the fluctuations between the electricity production and consumption when using renewable energy sources. Thanks to their flexibility, the SOCs can be operated in both fuel cell (SOFC for solid oxide fuel cell) and electrolysis (SOEC for Solid Oxide Electrolysis Cell) modes. They are composed of a dense electrolyte sandwiched between two porous electrodes. The so-called hydrogen electrode is typically a cermet composed of Yttria Stabilized Zirconia and Nickel (Ni-YSZ). Within the electrode, the dihydrogen and steam gaseous molecules are transported through the percolated porosity while the ionic and electronic conductivity for the oxygen ions and electrons is ensured by the YSZ and Ni phases, respectively. The electrochemical reactions takes place at the triple phase boundary (TPB) lines where the gas, electronic and ionic phases meet. Therefore, the SOCs electrochemical performances are strongly dependent on the electrode microstructural properties [1], and in particular some specific geometrical characteristics [2–4]. Moreover, in operation at high temperature, the hydrogen electrode is subjected to a phenomenon of Ni migration and agglomeration, which tends to decrease the density of TPB lines and hence the cell electrochemical performances [5, 6].

The characterization of the complex electrode microstructure is thus essential to better understand the initial electrode performances as well as the degradation mechanisms. For this purpose, different characterization techniques such as Focused Ion Beam coupled with a Scanning Electron Microscope (FIB-SEM) [7–9], X-ray absorption tomography [10–12] or X-ray holotomography [5, 13, 14] have been used to image the Ni-YSZ electrode in its pristine state or after long-term operation. Despite the possibility to reconstruct volumes at high resolution, this approach requires the manufacturing and testing of several cells in different operating conditions. The number of volumes are usually limited since the 3D characterization is time consuming. In this approach, the experimental dataset is in general insufficient to draw precise correlations on the impact of the electrode microstructure on SOCs performances and durability in different operating conditions.

*Corresponding author
Email addresses: l.theodon@emse.fr (L. Théodon), jerome.laurencin@cea.fr (J. Laurencin), Maxime.HUBERT@cea.fr (M. Hubert), cloetens@esrf.eu (P. Cloetens), debayle@emse.fr (J. Debayle)

Nomenclature

i, j	Phase name	ξ_{TPBl}	Density of Triple Phase Boundary length (μm^{-2})
C_i	Covariance function of i	τ_i^{geo}	Geometric tortuosity
ε_i	Volume fraction	β_i	Constrictivity
S_p^i	Specific surface area (μm^{-1})	M_i	Microstructure-factor
$S_p^{i,j}$	Interfacial specific surface area (μm^{-1})	d_p^i	Mean phase diameter (μm)
$P(\lambda)$	Poisson distribution	δ_i	Proportion of connected phase
$\#X$	Number of elements of a set X		

In order to overcome this problem, the development of model allowing the generation of synthetic microstructures has met a growing interest. Thus, many models have been already proposed in recent years, allowing the generation of representative microstructures for which the geometrical characteristics match the real electrode properties. Some of these models are based on non-overlapping hard spheres packing [15–19]. In this case, the microstructure is generated using an iterative process that can be relatively time-consuming. Other models are based on random Gaussian fields [20–24] or even random graphs [25]. They allow generating microstructures in a shorter time since no iterative procedures are involved for these simulations. All the proposed models offer rather good results, in particular for the modeling of globally homogeneous microstructures. Nevertheless, when the microstructure presents some local heterogeneities, some characteristics such as the microstructure factor, the geometrical tortuosity or the constrictivity, along with the continuous Phase Size Distributions (PSD), can be difficult to approach with high accuracy.

It is worth noting that the microstructure tends to be more and more heterogeneous after operation at high temperature due to the microstructural evolutions occurring in the electrode. Thus, taking into account this temporal evolution of the microstructure in order to optimize the performance and durability of SOCs is essential. Some physically based models have been already proposed to simulate in 3D this time evolution of the microstructure. In this frame, the phase-field approach has been recently used to simulate the Ni coarsening in operation [26–29]. However, this type of models requires very long computation time, limiting both the number of simulations and the volume of the studied microstructure. In this context, the development of geometrical models able to reproduce correctly the microstructural evolution upon operation is necessary and fully complementary with the physically based models. Indeed, the geometrical approach does not require large computational resources. Besides, the model does not depend on the material physicochemical properties and can be thus applied to any three-phase microstructure. However, to the best of our knowledge, no geometrical model has been proposed yet to simulate the microstructural evolution of SOC electrodes.

In this context, a Stochastic Time Evolution Microstructure (STEM) model has been developed for three-phase material and applied to the Ni-YSZ cermet for SOC application. The model is composed a of a static component, later called "static model", able to simulate the initial and final state of the same microstructure, and a dynamic component, able to simulate the temporal evolution of the microstructure between these two static bounds. This model is based on a degenerate random graph structure, similar to the one proposed by M.Neumann et al. [25], in which a temporal dimension has been added.

In a first part, the real electrode reconstructions and the microstructural properties measured on the 3D volumes are presented. In a second part, the static model is defined, followed by the STEM model, as well as examples of synthetic microstructure simulations. The optimization process used to identify the model parameters is also explained and validated. The static model is then calibrated and validated on two real Ni-YSZ microstructures obtained before and after ageing. The ability of the STEM model to reproduce the microstructural evolution is validated thanks to two other electrode reconstructions obtained at two intermediate times. The results including the evolution of the geometrical characteristics over the time are presented for the synthetic microstructures. Finally, the performances and limitations of the STEM model are discussed.

2. Image reconstruction and characterization

2.1. Image reconstruction

In this article, the Ni-YSZ cermet of a typical SOC were reconstructed by synchrotron X-ray holotomography [30, 31] before and after operation. This technique allows the acquisition of 3D volumes with a large field of view (50 μm) by keeping a resolution of a few tenth of a nanometer [32]. Fig. 1 shows three 3D reconstructions of real microstructures for three different operating times, with a voxel size of 50 nm. The protocol used to record the data and the procedure to reconstruct the electrode microstructures are thoroughly described in [32, 33]. It is worth noting that the studied images were obtained from cells manufactured in the same conditions and operated at T = 850°C for t = 0, 1000, 1500 and 2000 hours. All the details about the operating conditions as well as the reconstructions have been already published in [5].

2.2. Image characterization

The characterization of a 3D image consists in measuring a number of properties on it. A 3D volume representing the complex electrode microstructure is thus considered fully characterized once these properties are known. The most frequently measured properties are detailed in [21, 25] whereas the method

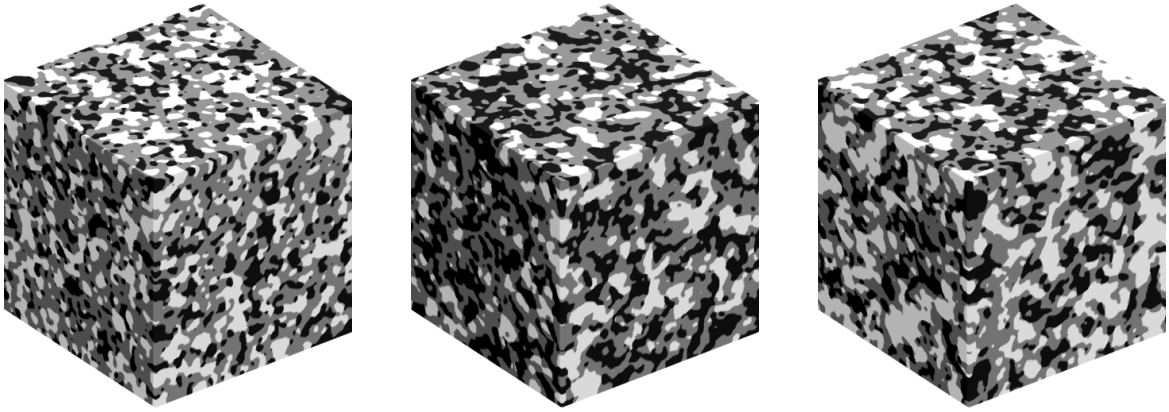

Figure 1. 3D reconstruction of three real microstructures. Cubes of 12.5 μm side (250^3 voxels). From left to right, the operating time of the cell is 0 h, 1500 h and 2000 h. The porous, YSZ and Ni phase are respectively black, gray and white.

for their computation is described in [31, 34]. The properties used in this article are listed below.

1. The phase volume fraction ε_i is the proportion of phase i to the total volume. It is simply computed by dividing the number of voxels belonging to phase i by the total number of voxels.
2. The proportion of connected phase δ_i is determined by computing the proportion of phase connecting two opposite sides of the total volume [34].
3. The density of Triple Phase Boundary length (TPBl) ξ_{TPBl} is computed by identifying each voxel edges at the triple contacts. A correction factor must be applied to take into account the cubic discretization of the domain in the form of voxels [31].
4. The specific surface areas S_p^i and interfacial specific surface areas $S_p^{i,j}$ correspond to the normalized area of phase i and the normalized area at the interface of phases i and j. They are computed as described in [35].
5. The tortuosity is a property fully described in [36]. The geometric tortuosity τ_i^{geo} computed for each of the phases i is equal to the ratio of the minimum distance to connect one side to the opposite side of the volume within the phase, to the length of the volume in that direction. In other words, if the length of the volume in a given direction is denoted l and l_m is the minimum length to go from one side of the volume to the other in that direction within phase i, then the following applies:
$$\tau_i^{geo} = l_m/l. \tag{1}$$
The minimum length l_m is computed using Dijkstra's algorithm on a Fibonacci heap structure [37–39].
6. The continuous Phase Size Distributions (PSD) or granulometry is computed by performing a sequence of morphological operations, namely morphological openings, using a homothetic sphere as structuring element as described in [31, 40].
7. The constrictivity β_i is a property that measures bottleneck effects of a given microstructure [3, 41]. It is based on the PSD, and therefore depends on the granulometry of the microstructure. It is defined as follows:
$$\beta_i = (r_{i,\min}/r_{i,\max})^2 \tag{2}$$
with $r_{i,\max}$ the maximum radius of the spheres allowing to fill at least 50% of phase i, i.e. the median of the cumulative PSD, noted d_p^i, and $r_{i,\min}$ the maximum radius of the spheres allowing to fill at least 50% of phase i by intrusion in a given transport direction. The quantity $r_{i,\min}$ can be computed using a Mercury Intrusion Porosimetry (MIP) simulation described in [41, 42] or derived from the PSD.
8. The microstructure-factor M_i of phase i in a given transport direction is defined as follows:
$$M_i = \sigma_i^e/\sigma_i^0 \tag{3}$$
where σ_i^e and σ_i^0 are respectively the effective and intrinsic conductivities for the percolated phase i. Note that for Ni-YSZ cermet electrodes, an empirical law has been proposed to relate the M-factor to the volume fraction, the constrictivity and the geometrical tortuosity [43] in the form:
$$M_i = \varepsilon_i^{1.67-0.48\beta_i} / \left(\tau_i^{geo}\right)^{5.18}. \tag{4}$$
9. The covariance function $C_i(r)$ of a phase i in a given direction contains information on the spatial structure and regularity of the microstructure, and in particular the volume fraction of the given phase [40]. It is defined as the probability that two points separated by a distance r belong to the same phase i. In particular, the following applies: $C_i(0) = \varepsilon_i$.

It can be noticed that many properties such as the tortuosity are dependent on the transport direction if considering anisotropic media. Nevertheless, it has been found that the values of tortuosity, M-factor, constrictivity, or covariance, had no preferred direction for typical electrode microstructures studied throughout this paper. As an illustration, Fig. 2 shows the covariance functions computed on four different 3D reconstructions of real microstructures along the three main axis. It appears clearly that these values do not depend on the considered axis proving that the real microstructures are isotropic.

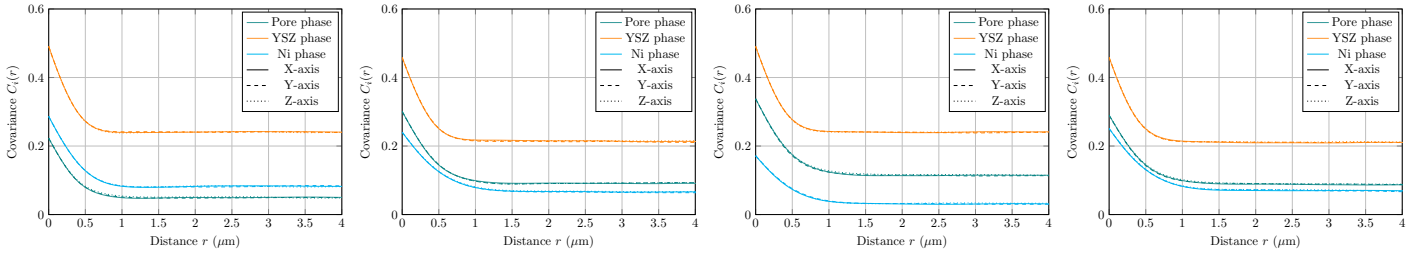

Figure 2. Covariance functions computed on 3D reconstructions of real microstructures. From left to right, the operating time of the SOC is $t = 0$ h, $t = 1000$ h, $t = 1500$ h and $t = 2000$ h.

Finally, the choice of the studied characteristics are motivated by their significance with respect to the effective transport properties of each phase in the heterogeneous microstructure. This is particularly the case for volume fraction, tortuosity and constrictivity [2, 3]. The density of TPBls is also a crucial parameter controlling the electrochemical reaction in the Ni-YSZ cermet [44].

3. Proposed stochastic geometrical model

3.1. Static model

The static model, which is proposed in this work to simulate three-phase electrode microstructures, is based on three independent point processes. The sets of points X_P, X_{YZS} related to the porosity and YSZ phase are generated using two Poisson processes [45] of intensity λ_P and λ_{YSZ} respectively. For the Ni phase, the set of points X_{Ni} is obtained using a Neyman-Scott point process [46]. This method allows generating sets of clustered points [47, 48] controlled by three parameters. Indeed, the method depends on (*i*) an intensity parameter λ_{Ni} for the centers of the clusters, (*ii*) a parameter σ for the standard deviation of a normal distribution that controls the dispersion around the centers of the clusters, and (*iii*) a parameter λ_c for the Poisson distribution providing the number of points per cluster. The Neyman-Scott point process has been selected to produce aggregated sets of points, which should be well adapted to reproduce accurately the phenomena of Ni agglomeration and depletion in the microstructure. The choice of this method for the Nickel phase is thoroughly justified and discussed in section 3.3.

After the generation of the random point patterns, it is worth noting that no graph related to the three electrode phases is built, in contrast to the method proposed by M.Neumann et al. [25]. In our case, each voxel in the volume V is directly associated to the set of points X_P, X_{YZS} or X_{Ni} in such a way that the distance between the voxel position and the set of points is minimal. In other words, the voxel is assigned to the phase related to the closest set of points using the method described in [49] to compute the three distance maps. Finally, a two-step Gaussian pseudo-smoothing parameter θ described in [25] is applied to the microstructure, which allows in particular to control the density of TPBl. The proposed static model thus depends on six parameters.

Examples of synthetic microstructures are shown in Fig. 3. It appears clearly that it is possible to control the local heterogeneity of the microstructure by adjusting respectively the density and size parameters, λ_{Ni} and λ_c, of the clusters for the Nickel phase (white phase).

3.2. STEM model

To represent the temporal evolution of the microstructure, the Stochastic Time Evolution Microstructure (STEM) model is based on the interpolation between two different states obtained with the static model (cf. previous section 3.1). The sets of parameter used to generate these two bounds are denoted $\omega^0 = \{\lambda_P^0; \lambda_{YSZ}^0; \lambda_{Ni}^0; \lambda_c^0; \sigma^0; \theta^0\}$ and $\omega^1 = \{\lambda_P^1; \lambda_{YSZ}^1; \lambda_{Ni}^1; \lambda_c^1; \sigma^1; \theta^1\}$ while the interpolation parameter evolving between these two states is denoted $t \in [0; 1]$.

Three sets of points $X_P(t)$, $X_{YSZ}(t)$ and $X_{Ni}(t)$ can be generated for each $t \in [0; 1]$ by interpolation as follows. A set X_0 (respectively X_1) is generated using the density $\max(\lambda_P^0, \lambda_P^1)$ (respectively $\max(\lambda_{YSZ}^0, \lambda_{YSZ}^1)$). Assuming that $\lambda_P^0 > \lambda_P^1$, the states $X_P(t = 0)$ and $X_P(t = 1)$ are defined such that $X_P(t = 0) = X_0$ and $\#X_P(t = 1) \sim P(\lambda_P^1)$, with $P(\lambda_P^1)$ a Poisson distribution of parameter λ_P^1. The set $X_P(t = 1)$ is built from $X_P(t = 0)$ by removing randomly a sufficient number of random points. The number of elements between $X_P(t = 0)$ and $X_P(t = 1)$ decreases linearly so that $X_P(t) \subseteq X_P(t = 0)$, $\forall t \in [0; 1]$. The process is symmetrical in the case where $\lambda_P^0 < \lambda_P^1$ and is identical for the definition of $X_{YSZ}(t)$. Thus, there is no spatial interpolation in the construction of the sets $X_P(t)$ and $X_{YSZ}(t)$.

Then, for the construction of the set $X_{Ni}(t)$, two sets $X_m(t = 0)$ and $X_m(t = 1)$ are generated using the cluster densities λ_{Ni}^0 and λ_{Ni}^1 respectively. These two sets represent the positions of the cluster centers of the Nickel phase in the microstructure for the two bounds at $t = 0$ and $t = 1$. Using the Auction Algorithm [50], it is possible to match the sets $X_m(t = 0)$ and $X_m(t = 1)$. The sum of the distances that must be covered by the center of the cluster to go from one state to the other is therefore minimal. The states $X_m(t)$ are finally defined by spatial interpolation between $X_m(t = 0)$ and $X_m(t = 1)$. The elements of $X_m(t = 0)$ that could not be matched with any element of $X_m(t = 1)$, and vice versa, are removed randomly according to the value of $t \in [0; 1]$ so that $\#X_m(t)$ varies linearly.

Finally, for each subset of points clustered around an element of $X_m(t)$, the same procedure as described above for the sets $X_P(t)$ and $X_{YSZ}(t)$ is performed, using the densities λ_c^0 and

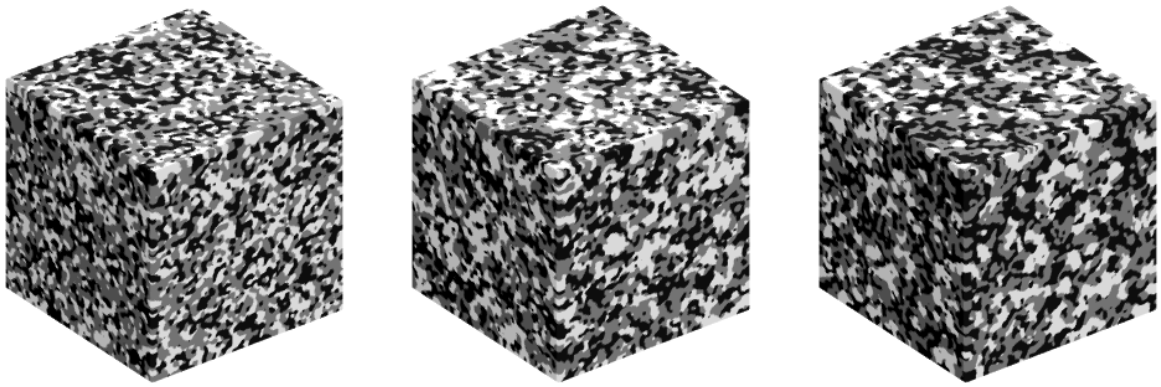

Figure 3. 3D rendering volume of three synthetic microstructures. Cubes of 17.5 μm side (350^3 voxels). From left to right, the parameters $\lambda_P = \lambda_{YZS} = 2.10^{-3}$, $\theta = 3$ and $\sigma = 5$ are constants, whereas $\lambda_{Ni} \in \{2.10^{-3}; 1.10^{-4}; 5.10^{-5}\}$ and $\lambda_c \in \{1; 20; 40\}$. The porous, YSZ and Ni phase are respectively black, gray and white.

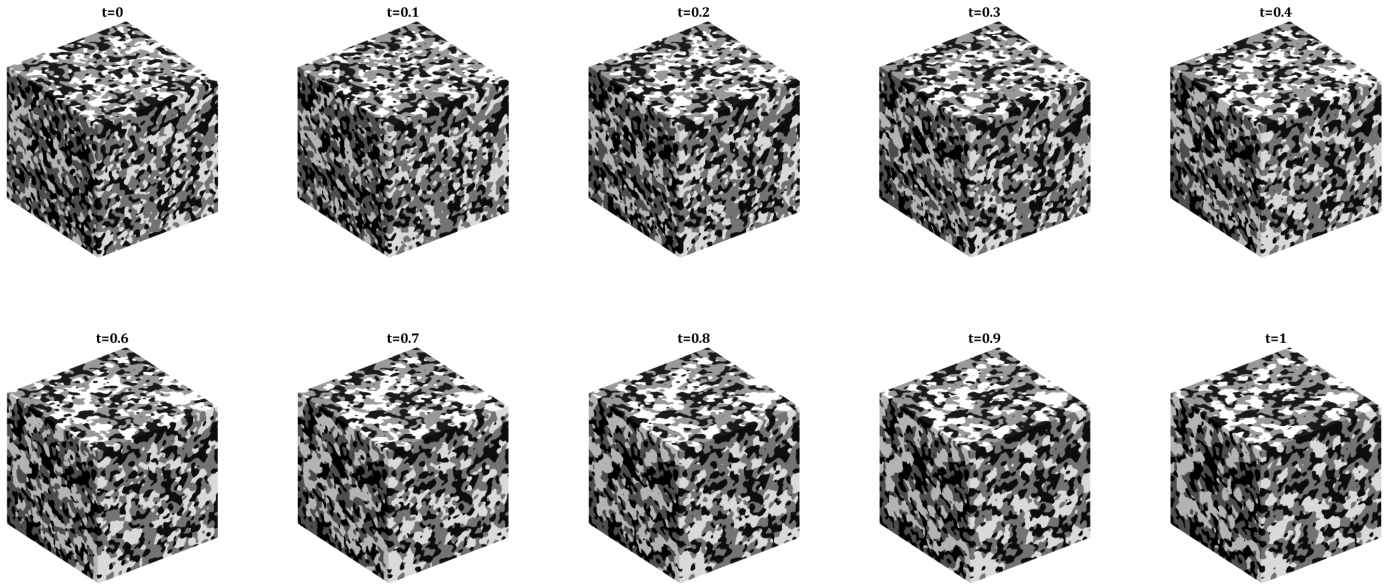

Figure 4. Evolution of the synthetic 3D microstructure between two states with the STEM model. Cubes of 12.5 μm side (250^3 voxels). Boundary states are given by $\omega^0 = \{2.10^{-3}; 2.10^{-3}; 1.10^{-4}; 15; 10; 3\}$ and $\omega^1 = \{2.10^{-3}; 2.10^{-3}; 5.10^{-5}; 50; 5; 3\}$. The porous, YSZ and Ni phase are respectively black, gray and white.

λ_c^1. The standard deviation of the distances of each of the generated point clusters around each center is itself adjusted so that it is equal to $\sigma(t) = t \times \sigma^1 + (1 - t) \times \sigma^0$. A set of points $X_{Ni}(t)$ can thus be defined as the set of points surrounding the set of cluster centers $X_m(t)$.

By definition, the three sets $X_P(t = 0)$, $X_{YSZ}(t = 0)$ and $X_{Ni}(t = 0)$ (resp. $X_P(t = 1)$, $X_{YSZ}(t = 1)$ and $X_{Ni}(t = 1)$) allow generating a microstructure with the same characteristics as the one generated with the parameter set ω^0 (resp. ω^1), once the smoothing parameter θ^0 (resp. θ^1) is applied. Therefore, it is possible to produce any intermediate state of the microstructure for $t \in [0; 1]$ using the $X_P(t)$, $X_{YSZ}(t)$ and $X_{Ni}(t)$ sets and applying a smoothing of parameter evolving with the time as follows:

$$\theta(t) = t \times \theta^1 + (1 - t) \times \theta^0. \quad (5)$$

Fig. 4 illustrates the results obtained by applying the STEM model to two states of the cermet microstructure in order to simulate the coalescence of the Nickel phase (white). It can be seen that it is mainly the Nickel phase that is moving by model design, which makes the transformation realistic.

3.3. Discussion

There are several reasons why it was decided to use a Neyman-Scott point process for the Ni phase rather than a Poisson point process. Initially, it was decided to combine graph matching techniques described in [51, 52] for the dynamic aspect of the model with the graph structure described in [25] for the static part. Nevertheless, it soon became apparent that it was possible to generate microstructures with satisfactory properties while using an underlying graph structure with an extremely small number of edges. Indeed, comparative tests involving synthetic microstructures generated from full graphs on the one hand and from their set of vertices only on the other hand have shown relative error differences of the order of 0.1% at most for all the measured geometrical properties. Therefore, the choice was made to leave the graph structure aside and to build the model

only on sets of points, i.e. the sets of vertices of degenerate graphs (cf. description of the static model 3.1). Thanks to this choice, it was possible to reduce the number of model parameters from ten to four. On the other hand, contrary to the microstructures studied in [25], those emulated with the STEM model are not necessarily locally homogeneous or fully connected [1, 29]. These characteristics are essential to simulate the phenomenon of the Nickel coarsening and agglomeration. Indeed, it seemed natural to use an aggregated point process to structure the Nickel phase, knowing that the analytical relationships between the model parameters and the geometrical properties of the microstructure could not be preserved.

Another reason that motivated the use of the Neyman-Scott point process is the evolutionary aspect of the microstructure. In the first version of the model, with an underlying graph structure, the different graphs representing a kind of skeleton of the microstructure were matched by solving a quadratic assignment problem [53], using the FAQ (Fast Approximate Quadratic assignment problem) algorithm [54, 55]. However, the computation time can be very long on large volumes. Without the graph structure, the proposed model consists in solving a fast linear assignment problem [56]. Moreover, by using a Neyman-Scott point process, it was possible to further optimize the computation time by matching the sets of cluster centers rather than the whole sets of points associated with the Nickel phase, thus reducing the size of the sets to be matched by at least one order of magnitude.

Finally, it should be noted that the set matching process only applies to the Nickel phase. This choice not only reduces the computation time, but it is also motivated by the objective of obtaining a more realistic transformation. Indeed, by modifying only slightly the sets of points associated with the porous and ceramic phases of the microstructure, these phases themselves will only be marginally affected by the temporal evolution and the interpolation process. This behavior is more in line with reality, as can be seen in Fig. 4.

4. Models fitting and validation

4.1. Cost function and optimization process

The fitting process requires the definition of a cost function. Among the most interesting geometrical properties for optimizing the SOC performances, the choice was made to retain the density of TPBl, the interfacial specific surface areas and the volume fractions. For a set of parameter values ω for the STEM model and a set of geometric properties measured on the 3D reconstruction of an electrode, the proposed cost function is defined as follows.

$$F_k(\omega) = 4 \times \sum_{i=0}^{2} \Delta\left(\varepsilon_i\right) + \sum_{0 \le i < j \le 2} \Delta(S^{i,j}) + 2 \times \Delta(\xi_{\mathrm{TPBl}}) \qquad (6)$$

where Δ is the relative error on the geometric properties measured on the 3D synthetic microstructure generated by the STEM model with the set of parameter values ω and the geometric properties contained in the set k.

It should be noticed that the specific surface areas can be deduced by linear combination of the interfacial specific surface areas, the reverse not being true. For this reason, the interfacial specific surface areas have been chosen as parameters in the cost function.

The fitting process consists of applying the Covariance Matrix Adaptation Evolution Strategy (CMA-ES) algorithm [57, 58] to the cost function F_k for a set of properties k. To validate the approach, a synthetic microstructure was generated by the STEM model using a set of known parameter values ω_0. The necessary geometric properties were measured on this microstructure. The fitting process was then run, and a set of parameter values $\widehat{\omega}_0$ was obtained. Table 1 shows the relative errors between the elements of ω_0 and $\widehat{\omega}_0$. As the differences are extremely small, the fitting process is considered as validated.

Table 1. Comparison of the values used to generate a synthetic microstructure with those returned by the fitting process.

Parameters	Original values (ω_0)	Fitted values ($\widehat{\omega}_0$)	Error
λ_P	16 μm^{-3}	16.12 μm^{-3}	0.7%
λ_{YSZ}	16 μm^{-3}	15.91 μm^{-3}	-0.6%
λ_{Ni}	0.8 μm^{-3}	0.79 μm^{-3}	-0.6%
λ_c	20	19.81	-0.9%
σ	0.2 μm	0.21 μm	3.4%
θ	3	3.02	0.7%

4.2. Static model validation

In order to validate the static model, the fitting procedure was performed using data from several real microstructures. The quality of the model was mainly evaluated with respect to the errors made on the geometrical properties of the generated synthetic microstructure that are not taken into account in the cost function, such as the tortuosity or the constrictivity.

The rendering volumes for the reconstructions of the real microstructures and the related synthetic microstructures generated by the static model after the optimization step are displayed in Fig. 5. The two real microstructures correspond to the same type of Ni-YSZ cermet obtained for the pristine cell (t = 0 h) and after an operation of t = 2000 h. The measurements made on the corresponding real and synthetic microstructures are provided in Tables 2 and 3.

When comparing the geometrical properties of the real and synthetic microstructures, it appears that the results are in good agreement regarding the volume fractions and the density of TPBl (i.e. the properties that have the most weight in the cost function). The results are also satisfactory for the interfacial specific surface areas, even if the discrepancy on $S_p^{0,2}$ is higher. However, it can be noticed that the error on the specific surface areas between the real electrodes and the synthetic microstructures remains very limited. This implies a probable limitation of the model, which fails to take into account precisely the interaction between the phases. This error on $S_p^{0,2}$ is more pronounced for the aged electrode for which the Nickel phase is aggregated around clusters leading to enhance the local heterogeneity in the microstructure. As for the other properties, a good agreement

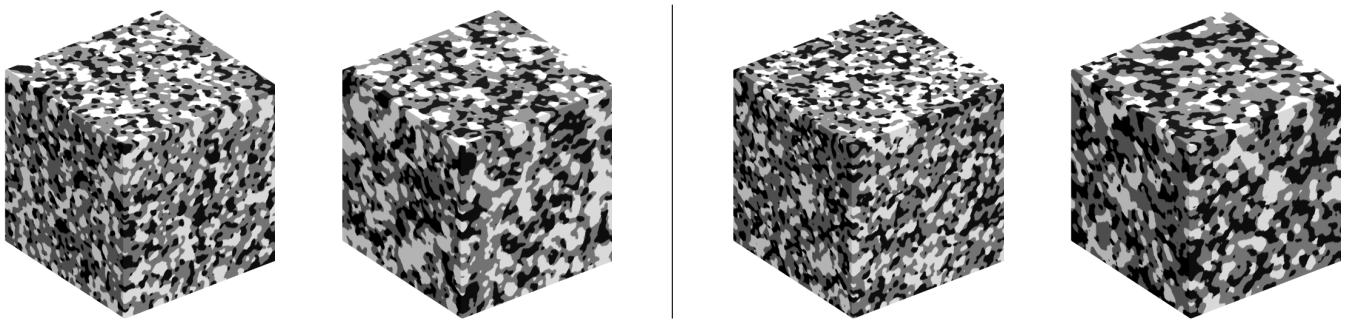

Figure 5. From left to right, 3D reconstruction of a real microstructure before use, after 2000 h of use, and synthetic microstructures generated by the static model after optimization (t = 0 h and t = 2000 h). Cube of 17.5 μm side. The porous, YSZ and Ni phase are respectively black, gray and white.

Electrode at t = 0 h

	Porous phase							Solid phase (YSZ)						
Properties	$S_p(\mu m^{-1})$	$\delta(\%)$	$\varepsilon(\%)$	$d_p(\mu m)$	$\tau^{geo}(-)$	$\beta(-)$	M-factor $(-)$	$S_p(\mu m^{-1})$	$\delta(\%)$	$\varepsilon(\%)$	$d_p(\mu m)$	$\tau^{geo}(-)$	$\beta(-)$	M-factor $(-)$
Real μ-structure	1.49	0.95	0.22	0.56	1.61	0.59	0.010	2.39	0.99	0.49	0.59	1.17	0.61	0.166
Virtual μ-structure	1.55	0.97	0.22	0.52	1.61	0.65	0.011	2.4	0.99	0.48	0.63	1.18	0.58	0.153
Error (%)	3.6%	2.9%	0.1%	7.1%	0.1%	10.6%	4.4%	0.1%	−0.8%	−0.8%	6.8%	−0.7%	4.5%	−7.9%
	Solid phase (Ni)													
Properties	$S_p(\mu m^{-1})$	$\delta(\%)$	$\varepsilon(\%)$	$d_p(\mu m)$	$\tau^{geo}(-)$	$\beta(-)$	M-factor $(-)$	$\xi_{TPBl}(\mu m^{-2})$	$S_p^{0,1}$	$S_p^{0,2}$	$S_p^{1,2}$			
Real μ-structure	1.56	0.97	0.29	0.67	1.47	0.6	0.024	2.42	1.22	0.33	1.16			
Virtual μ-structure	1.62	0.98	0.29	0.64	1.47	0.64	0.025	2.43	1.22	0.38	1.16			
Error (%)	3.8%	2.7%	0.1%	4.5%	0.4%	5.4%	2.4%	1.3%	0.2%	17%	−0.1%			

Table 2. Geometric properties of the 3D reconstructions of the real and synthetic microstructures.

Electrode at t = 2000 h

	Porous phase							Solid phase (YSZ)						
Properties	$S_p(\mu m^{-1})$	$\delta(\%)$	$\varepsilon(\%)$	$d_p(\mu m)$	$\tau^{geo}(-)$	$\beta(-)$	M-factor $(-)$	$S_p(\mu m^{-1})$	$\delta(\%)$	$\varepsilon(\%)$	$d_p(\mu m)$	$\tau^{geo}(-)$	$\beta(-)$	M-factor $(-)$
Real μ-structure	1.41	0.99	0.31	0.72	1.35	0.58	0.041	2.25	0.99	0.47	0.6	1.16	0.59	0.163
Virtual μ-structure	1.42	0.99	0.28	0.7	1.44	0.62	0.026	2.06	0.99	0.51	0.75	1.16	0.58	0.141
Error (%)	∼ 0%	0.6%	−8%	2.8%	7.3%	5.8%	−36%	−8.7%	∼ 0%	8.7%	25%	0.2%	1.7%	−13.5%
	Solid phase (Ni)													
Properties	$S_p(\mu m^{-1})$	$\delta(\%)$	$\varepsilon(\%)$	$d_p(\mu m)$	$\tau^{geo}(-)$	$\beta(-)$	M-factor $(-)$	$\xi_{TPBl}(\mu m^{-2})$	$S_p^{0,1}$	$S_p^{0,2}$	$S_p^{1,2}$			
Real μ-structure	1.05	0.92	0.22	0.8	1.65	0.56	0.009	1.11	1.3	0.11	0.94			
Virtual μ-structure	0.94	0.89	0.21	0.84	1.82	0.66	0.005	1.09	1.26	0.15	0.79			
Error (%)	−10.1%	−3%	−8%	5%	10.2%	16.5%	−39%	−1.8%	−3.4%	42.8%	−16%			

Table 3. Geometric properties of the 3D reconstructions of the real and synthetic microstructures.

between the synthetic microstructures and the real reconstructions is found for the proportion of connected phase, the geometrical tortuosity, the constrictivity and the M-factor, at least for the cell at t = 0 h. It can be noted that the error is higher for the M-factor of the aged electrode (t = 2000 h). This limitation on the microstructural factor is a recurrent problem that has been already reported in literature [15, 21, 25].

Finally, as a general matter, it can be concluded that the results are globally better with the first microstructure (t = 0 h) than with the second (t = 2000 h), in particular for the constrictivity, the tortuosity and the M-factor. As mentioned before, the model is more suited to microstructures with low local heterogeneity, which is not the case for the second microstructure, due to the agglomeration of the Nickel phase.

4.3. STEM model validation

The STEM model is able to simulate the evolution of the microstructure by interpolation between two known states that can be emulated with the static model. In this study, electrode reconstructions are available for cells operated at the same temperature at different ageing times $t \in \{0\,\text{h}; 1000\,\text{h}; 1500\,\text{h}; 2000\,\text{h}\}$. Although it is possible to use the static model to generate microstructures fitted for these four operating times, the STEM model is designed to predict the microstructure evolution between the two bounds for which it was calibrated (i.e. with $t \in [0; 2000]$). To validate the STEM model, the microstructural properties measured on the synthetic volumes at different operating times must be compared to the ones extracted from the reconstructions.

Fig. 6 shows the temporal evolution of a 3D microstructure generated by the STEM model for $t \in [0; 2000]$. In Fig. 7, some properties taken from the synthetic volumes are plotted as function of time and compared with the real data. At the same time, Tables 4 and 5 compile all the properties measured on the real microstructures and the microstructures generated by the STEM model. They also include the properties extracted from 3D microstructures obtained with the static model by fitting its parameters to the real data.

First, Fig. 7 shows that over a set of six STEM simulations, the standard deviation of the measured properties is extremely

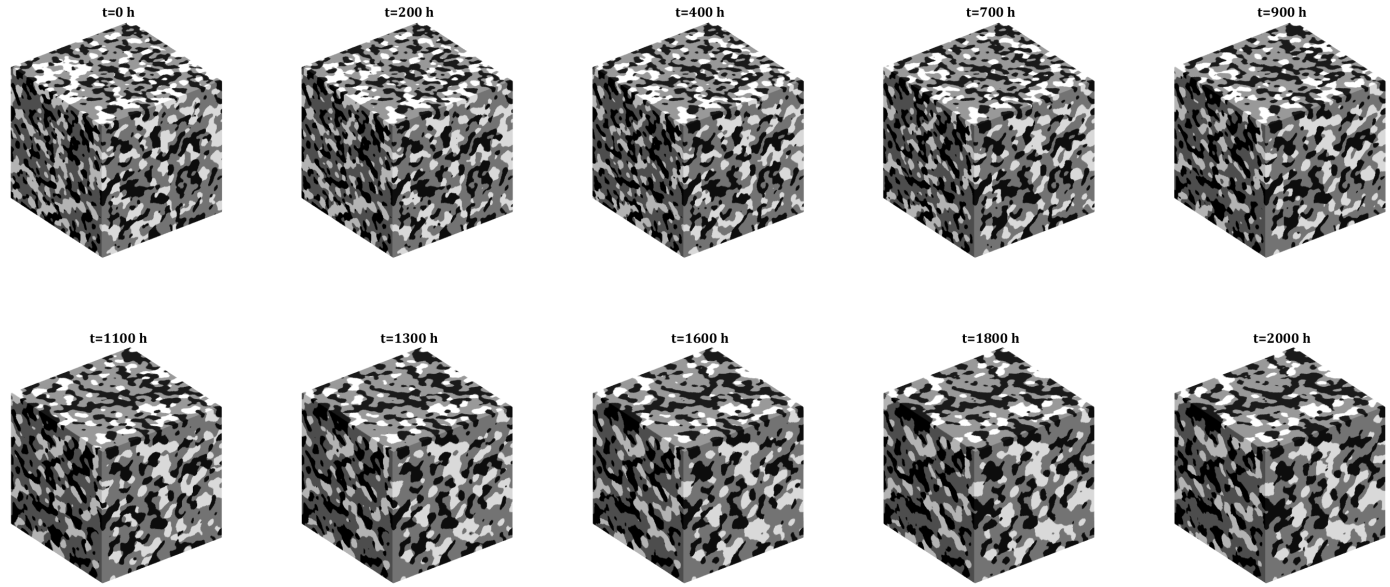

Figure 6. Evolution of the microstructure generated by the STEM model by interpolation between two extreme states fitted to real data. Cubes of 12.5 μm side (250^3 voxels). The porous, YSZ and Ni phase are respectively black, gray and white.

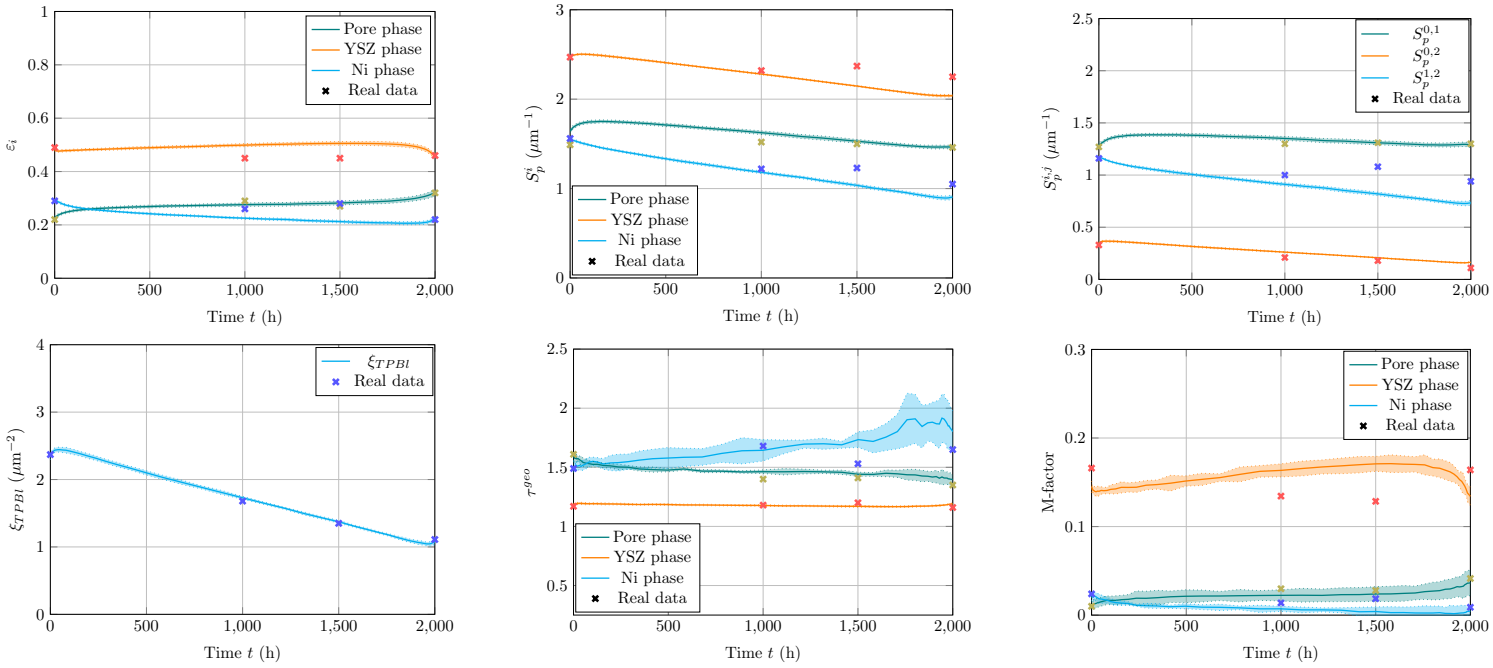

Figure 7. Evolution of the properties of the synthetic microstructure generated by the STEM model throughout the lifecycle of the SOC (from t = 0 h to t = 2000 h). The properties are computed over an average of 6 simulations. The dotted lines correspond to the standard deviation. Measurements made on 3D reconstructions of real microstructures are also indicated.

Electrode at t = 1000 h

	Porous phase							Solid phase (YSZ)						
Properties	$S_p(\mu m^{-1})$	$\delta(\%)$	$\varepsilon(\%)$	$d_p(\mu m)$	$\tau^{geo}(-)$	$\beta(-)$	M-factor (−)	$S_p(\mu m^{-1})$	$\delta(\%)$	$\varepsilon(\%)$	$d_p(\mu m)$	$\tau^{geo}(-)$	$\beta(-)$	M-factor (−)
Real μ-structure	1.52	0.99	0.29	0.41	1.4	0.5	0.029	2.32	0.99	0.45	0.36	1.18	0.48	0.134
Static model	1.46	0.99	0.29	0.44	1.42	0.53	0.028	2.2	0.99	0.45	0.44	1.18	0.49	0.134
STEM model	1.63	0.98	0.28	0.35	1.45	0.49	0.023	2.28	0.99	0.5	0.43	1.17	0.51	0.165
Error static (%)	−3.9%	0.2%	−0.9%	7.3%	−1%	5.7%	−5.4%	−4.8%	∼ 0%	−0.2%	19.4%	−0.2%	0.9%	0.3%
Error STEM (%)	3.4%	−0.5%	−2.3%	−14.6%	2.8%	−2%	−21%	−1.5%	∼ 0%	11%	18%	−0.8%	5.6%	22.8%
	Solid phase (Ni)													
Properties	$S_p(\mu m^{-1})$	$\delta(\%)$	$\varepsilon(\%)$	$d_p(\mu m)$	$\tau^{geo}(-)$	$\beta(-)$	M-factor (−)	$\xi_{TPBl}(\mu m^{-2})$	$S_p^{0,1}$	$S_p^{0,2}$	$S_p^{1,2}$			
Real μ-structure	1.22	0.95	0.26	0.51	1.58	0.53	0.014	1.68	1.3	0.21	1.0			
Static model	1.24	0.97	0.26	0.48	1.63	0.63	0.013	1.68	1.21	0.25	0.98			
STEM model	1.18	0.91	0.23	0.46	1.73	0.57	0.007	1.73	1.35	0.26	0.91			
Error static (%)	1.8%	3.1%	−0.9%	5.9%	−3.2%	19.1%	−9.2%	0.1%	−7.4%	17.4%	−1.5%			
Error STEM (%)	−2.7%	−3.6%	−13%	−10%	9.8%	8.4%	−46%	2.9%	3.6%	24.6%	−8.7%			

Table 4. Geometric properties of the 3D reconstructions of the real and synthetic microstructures. Comparison between the properties of the real microstructure, those of the microstructure generated by the static model, and those of a microstructure generated by the STEM model.

Electrode at t = 1500 h

	Porous phase							Solid phase (YSZ)						
Properties	$S_p(\mu m^{-1})$	$\delta(\%)$	$\varepsilon(\%)$	$d_p(\mu m)$	$\tau^{geo}(-)$	$\beta(-)$	M-factor (−)	$S_p(\mu m^{-1})$	$\delta(\%)$	$\varepsilon(\%)$	$d_p(\mu m)$	$\tau^{geo}(-)$	$\beta(-)$	M-factor (−)
Real μ-structure	1.5	0.99	0.27	0.61	1.41	0.62	0.028	2.41	0.99	0.45	0.56	1.2	0.59	0.128
Static model	1.38	0.98	0.27	0.69	1.5	0.61	0.020	2.06	0.99	0.45	0.71	1.21	0.6	0.123
STEM model	1.53	0.99	0.28	0.59	1.44	0.61	0.026	2.21	0.99	0.5	0.71	1.19	0.65	0.158
Error static (%)	−8%	−0.7%	0.9%	13.1%	−6.3%	1.1%	−28%	−14.7%	∼ 0%	−0.2%	26.8%	1.1%	1.8%	−3.8%
Error STEM (%)	2.1%	0.7%	3.7%	−3.6%	2.1%	−0.8%	−6.3%	−9.1%	∼ 0%	11%	26.7%	−0.8%	9.9%	23%
	Solid phase (Ni)													
Properties	$S_p(\mu m^{-1})$	$\delta(\%)$	$\varepsilon(\%)$	$d_p(\mu m)$	$\tau^{geo}(-)$	$\beta(-)$	M-factor (−)	$\xi_{TPBl}(\mu m^{-2})$	$S_p^{0,1}$	$S_p^{0,2}$	$S_p^{1,2}$			
Real μ-structure	1.28	0.94	0.28	0.85	1.53	0.57	0.018	1.35	1.31	0.18	1.08			
Static model	1.25	0.96	0.28	0.78	1.55	0.69	0.018	1.36	1.08	0.28	0.96			
STEM model	1.23	0.93	0.23	0.83	1.66	0.68	0.010	1.36	1.36	0.27	0.95			
Error static (%)	−1.7%	2.1%	0.9%	8.2%	−1.4%	22.5%	0.6%	0.3%	−17.3%	59.7%	−11.7%			
Error STEM (%)	−3.8%	−0.7%	−17%	−1.3%	8.8%	19%	−46%	0.9%	−7.4%	50.5%	−12%			

Table 5. Geometric properties of the 3D reconstructions of the real and synthetic microstructures. Comparison between the properties of the real microstructure, those of the microstructure generated by the static model, and those of a microstructure generated by the STEM model.

small, except for the geometrical tortuosity of the Nickel phase. This last result is probably correlated with the fact that only the set of points providing the structure of the Nickel phase is mobile due to the agglomeration. Regarding the tortuosity, it can be noted that the one of the YSZ phase is almost constant over time, which is explained by the stability of the ceramic phase in operation. The STEM model is not without limitations if considering the comparison between the volume fractions, specific surface areas and interfacial specific surface areas for the synthetic and real microstructures at t = 1000 h and t = 1500 h. However, it is worth noting that the variations of these properties, sometimes significant and unintuitive for the real microstructures, come from the fact that the data are extracted from four different microstructures, and not from the same SOC whose properties were measured at four different times in its lifespan.

Tables 4 and 5 show in more details the relative discrepancies that arise between the properties of real microstructures and those that the STEM model can generate. It can be seen that some parameters such as the density of TPBl, the specific surface areas and, to a lesser extent, the interfacial specific surface areas, are rather well predicted by the model. The volume fractions are also sometimes a little off the mark, especially for the YSZ phase, although the deviation is rarely greater than 10%. The structural properties such as the M-factor, tortuosity, constrictivity or mean phase diameter are also rather well approximated if the errors are put in perspective with those generally reported in literature [15, 21, 22, 25].

Overall, the curves representing the temporal evolution of the microstructural properties generated by the STEM model (Fig. 7) are rather smooth and continuous, with the notable exception of the tortuosity of the Nickel phase. As a general comment, the deviations from the real data are usually in the range of 10% at the most, with the exception of the specific case of $S_p^{0,2}$ already mentioned in section 3.1. This rather good agreement between the evolutions of real and synthetic microstructures tends to validate the model. Indeed, the STEM model is able to generate three-phase microstructures at each moment of the SOC lifetime between two known boundary states. Although the properties of the synthetic microstructures sometimes deviate slightly from the real data, their evolution is rather smooth, with the understanding that the model can still be greatly improved. Indeed, it should be noted that an area for improvement would be to reconsider the way in which the interpolation between the two extreme bounds is performed. In fact, it has been stressed that many parameters, such as the number of elements of the sets of points structuring the three phases, the cluster dispersion parameter of the Neyman-Scott point process or the smoothing parameter of the microstructure, should evolve in a linear way. This choice is obviously questionable and more

accurate evolutions based on physical considerations could be implemented in the STEM model. Nevertheless, the STEM approach constitutes a relevant framework to obtain geometrical models able to reproduce correctly the microstructural evolution of SOC electrodes.

5. Conclusion

In this paper, an original model named STEM has been proposed to simulate the evolution of a SOC microstructure by interpolation between two known states. These bounds are simulated using a static model based on sets of random points. Special care was paid to optimize the process of microstructure generation and its evolution over time. Indeed, the generation of a microstructure with the static model takes only a few seconds, while the simulation of its temporal evolution with the STEM model takes only a few minutes. The static model showed that it is able to generate virtual microstructures whose geometrical characteristics are close to the real microstructures. The STEM model is able to simulate the continuous evolution of these characteristics. The most important discrepancies can be explained (*i*) by the simplicity and lack of flexibility of the static model, (*ii*) the improvements that still need to be made to the STEM model, and (*iii*) the fact that the experimental data at our disposal do not represent the temporal evolution of a single SOC (but were taken from four different SOCs of the same batch operated under the same conditions at different times).

Acknowledgment

The author(s) acknowledge(s) the support of the French Agence Nationale de la Recherche (ANR), under grant ANR-18-CE05-0036 (project ECOREVE).

References

[1] B. Shri Prakash, S. Senthil Kumar, S. Aruna, Properties and development of Ni/YSZ as an anode material in solid oxide fuel cell: A review, Renewable and Sustainable Energy Reviews 36 (C) (2014) 149–179. doi:10.1016/j.rser.2014.04.04.

[2] L. Holzer, B. Iwanschitz, T. Hocker, L. Keller, O. Pecho, G. Sartoris, P. Gasser, B. Muench, Redox cycling of ni–ysz anodes for solid oxide fuel cells: Influence of tortuosity, constriction and percolation factors on the effective transport properties, Journal of Power Sources 242 (2013) 179–194. doi:https://doi.org/10.1016/j.jpowsour.2013.05.047.

[3] G. Gaiselmann, M. Neumann, V. Schmidt, O. Pecho, T. Hocker, L. Holzer, Quantitative relationships between microstructure and effective transport properties based on virtual materials testing, AIChE Journal 60 (6) (2014) 1983–1999. arXiv:https://aiche.onlinelibrary.wiley.com/doi/pdf/10.1002/aic.14416, doi:https://doi.org/10.1002/aic.14416.

[4] E. Effori, H. Moussaoui, F. Monaco, R. K. Sharma, J. Debayle, Y. Gavet, G. Delette, G. Si Larbi, E. Siebert, J. Vulliet, L. Dessemond, J. Laurencin, Reaction mechanism and impact of microstructure on performances for the lscf-cgo composite electrode in solid oxide cells, Fuel Cells 19 (4) (2019) 429–444. arXiv:https://onlinelibrary.wiley.com/doi/pdf/10.1002/fuce.201800185, doi:https://doi.org/10.1002/fuce.201800185.

[5] M. Hubert, J. Laurencin, P. Cloetens, B. Morel, D. Montinaro, F. Lefebvre-Joud, Impact of nickel agglomeration on solid oxide cell operated in fuel cell and electrolysis modes, Journal of Power Sources 397 (2018) 240–251. doi:https://doi.org/10.1016/j.jpowsour.2018.06.097.

[6] A. Zekri, K. Herbrig, M. Knipper, J. Parisi, T. Plaggenborg, Nickel depletion and agglomeration in sofc anodes during long-term operation, Fuel Cells 17 (3) (2017) 359–366. arXiv:https://onlinelibrary.wiley.com/doi/pdf/10.1002/fuce.201600220, doi:https://doi.org/10.1002/fuce.201600220.

[7] J. R. Wilson, W. Kobsiriphat, R. Mendoza, H.-Y. Chen, J. M. Hiller, D. J. Miller, K. Thornton, P. W. Voorhees, S. B. Adler, S. A. Barnett, Three-dimensional reconstruction of a solid-oxide fuel-cell anode, Nature Materials 5 (7) (2006) 541–544. doi:10.1038/nmat1668.

[8] T. Matsui, J.-Y. Kim, H. Muroyama, M. Shimazu, T. Abe, M. Miyao, K. Eguchi, Anode microstructural change upon long-term operation for the cathode-supported tubular-type sofc (2012). doi:10.1016/J.SSI.2012.03.035.

[9] T. A. Prokop, K. Berent, H. Iwai, J. S. Szmyd, G. Brus, A three-dimensional heterogeneity analysis of electrochemical energy conversion in sofc anodes using electron nanotomography and mathematical modeling, International Journal of Hydrogen Energy 43 (21) (2018) 10016–10030. doi:https://doi.org/10.1016/j.ijhydene.2018.04.023.

[10] P. Shearing, J. Gelb, J. Yi, W.-K. Lee, M. Drakopolous, N. Brandon, Analysis of triple phase contact in ni–ysz microstructures using non-destructive x-ray tomography with synchrotron radiation, Electrochemistry Communications 12 (8) (2010) 1021–1024. doi:https://doi.org/10.1016/j.elecom.2010.05.014.

[11] G. J. Nelson, K. N. Grew, J. R. Izzo, J. J. Lombardo, W. M. Harris, A. Faes, A. Hessler-Wyser, J. Van herle, S. Wang, Y. S. Chu, A. V. Virkar, W. K. Chiu, Three-dimensional microstructural changes in the ni–ysz solid oxide fuel cell anode during operation, Acta Materialia 60 (8) (2012) 3491–3500. doi:https://doi.org/10.1016/j.actamat.2012.02.041.

[12] Y.-c. K. Chen-Wiegart, D. Kennouche, J. Scott Cronin, S. A. Barnett, J. Wang, Effect of ni content on the morphological evolution of ni-ysz solid oxide fuel cell electrodes, Applied Physics Letters 108 (8) (2016) 083903. arXiv:https://doi.org/10.1063/1.4942459, doi:10.1063/1.4942459.

[13] E. Lay-Grindler, J. Laurencin, J. Villanova, P. Cloetens, P. Bleuet, A. Mansuy, J. Mougin, G. Delette, Degradation study by 3d reconstruction of a nickel–yttria stabilized zirconia cathode after high temperature steam electrolysis operation, Journal of Power Sources 269 (2014) 927–936. doi:https://doi.org/10.1016/j.jpowsour.2014.07.066.

[14] F. Monaco, M. Hubert, J. Vulliet, J. P. Ouweltjes, D. Montinaro, P. Cloetens, P. Piccardo, F. Lefebvre-Joud, J. Laurencin, Degradation of ni-YSZ electrodes in solid oxide cells: Impact of polarization and initial microstructure on the ni evolution, Journal of The Electrochemical Society 166 (15) (2019) F1229–F1242. doi:10.1149/2.1261915jes.

[15] H. Moussaoui, J. Debayle, Y. Gavet, P. Cloetens, J. Laurencin, Particle-based model for functional and diffusion layers of solid oxide cells electrodes, Powder Technology 367 (2020) 67–81. doi:https://doi.org/10.1016/j.powtec.2020.03.040.

[16] C. Metcalfe, O. Kesler, T. Rivard, F. Gitzhofer, N. Abatzoglou, Connected three-phase boundary length evaluation in modeled sintered composite solid oxide fuel cell electrodes, Journal of The Electrochemical Society 157 (9) (2010) B1326. doi:10.1149/1.3459902.

[17] B. Kenney, M. Valdmanis, C. Baker, J. Pharoah, K. Karan, Computation of tpb length, surface area and pore size from numerical reconstruction of composite solid oxide fuel cell electrodes, Journal of Power Sources 189 (2) (2009) 1051–1059. doi:https://doi.org/10.1016/j.jpowsour.2008.12.145.

[18] J. Golbert, C. S. Adjiman, N. P. Brandon, Microstructural modeling of solid oxide fuel cell anodes, Industrial & Engineering Chemistry Research 47 (20) (2008) 7693–7699. arXiv:https://doi.org/10.1021/ie800065w, doi:10.1021/ie800065w.

[19] D. Westhoff, I. Manke, V. Schmidt, Generation of virtual lithium-ion battery electrode microstructures based on spatial stochastic modeling, Computational Materials Science 151 (2018) 53–64. doi:https://doi.org/10.1016/j.commatsci.2018.04.060.

[20] B. Abdallah, F. Willot, D. Jeulin, Morphological modelling of three-phase microstructures of anode layers using SEM images., Journal of microscopy 263 (1) (2016) 51–63. doi:10.1111/jmi.12374.

[21] H. Moussaoui, J. Laurencin, Y. Gavet, G. Delette, M. Hubert, P. Cloetens, T. Le Bihan, J. Debayle, Stochastic geometrical modeling of solid oxide cells electrodes validated on 3d reconstructions, Computational Materials Science 143 (2018) 262–276.

doi:https://doi.org/10.1016/j.commatsci.2017.11.015.
[22] B. Prifling, M. Ademmer, F. Single, O. Benevolenski, A. Hilger, M. Osenberg, I. Manke, V. Schmidt, Stochastic 3d microstructure modeling of anodes in lithium-ion batteries with a particular focus on local heterogeneity, Computational Materials Science 192 (2021) 110354. doi:https://doi.org/10.1016/j.commatsci.2021.110354.
[23] H. Moussaoui, J. Laurencin, M. Hubert, R. Sharma, P. Cloetens, G. Delette, Y. Gavet, J. Debayle, Stochastic geometrical and microstructural modeling for solid oxide cell electrodes, ECS Transactions 91 (1) (2019) 2031–2043. doi:10.1149/09101.2031ecst.
[24] H. Moussaoui, J. Debayle, Y. Gavet, G. Delette, M. Hubert, P. Cloetens, J. Laurencin, 3D geometrical characterization and modelling of solid oxide cells electrodes microstructure by image analysis, in: H. Nagahara, K. Umeda, A. Yamashita (Eds.), Thirteenth International Conference on Quality Control by Artificial Vision 2017, Vol. 10338, International Society for Optics and Photonics, SPIE, 2017, pp. 15 – 22. doi:10.1117/12.2264376.
[25] M. Neumann, J. Staněk, O. M. Pecho, L. Holzer, V. Beneš, V. Schmidt, Stochastic 3d modeling of complex three-phase microstructures in sofc-electrodes with completely connected phases, Computational Materials Science 118 (2016) 353–364. doi:https://doi.org/10.1016/j.commatsci.2016.03.013.
[26] T. Takaki, Phase-field modeling and simulations of dendrite growth, ISIJ International 54 (2) (2014) 437–444. doi:10.2355/isijinternational.54.437.
[27] Y. Lei, T.-L. Cheng, H. Abernathy, W. Epting, T. Kalapos, G. Hackett, Y. Wen, Phase field simulation of anode microstructure evolution of solid oxide fuel cell through ni(oh)2 diffusion, Journal of Power Sources 482 (2021) 228971. doi:https://doi.org/10.1016/j.jpowsour.2020.228971.
[28] H.-Y. Chen, H.-C. Yu, J. Scott Cronin, J. R. Wilson, S. A. Barnett, K. Thornton, Simulation of coarsening in three-phase solid oxide fuel cell anodes, Journal of Power Sources 196 (3) (2011) 1333–1337. doi:https://doi.org/10.1016/j.jpowsour.2010.08.010.
[29] Z. Jiao, N. Shikazono, Simulation of nickel morphological and crystal structures evolution in solid oxide fuel cell anode using phase field method, Journal of The Electrochemical Society 161 (5) (2014) F577–F582. doi:10.1149/2.009405jes.
[30] J. Villanova, J. Laurencin, P. Cloetens, P. Bleuet, G. Delette, H. Suhonen, F. Usseglio-Viretta, 3d phase mapping of solid oxide fuel cell ysz/ni cermet at the nanoscale by holographic x-ray nanotomography, Journal of Power Sources 243 (2013) 841–849. doi:https://doi.org/10.1016/j.jpowsour.2013.06.069.
[31] J. Laurencin, R. Quey, G. Delette, H. Suhonen, P. Cloetens, P. Bleuet, Characterisation of solid oxide fuel cell ni–8ysz substrate by synchrotron x-ray nano-tomography: from 3d reconstruction to microstructure quantification, Journal of Power Sources 198 (2012) 182–189. doi:https://doi.org/10.1016/j.jpowsour.2011.09.105.
[32] M. Hubert, A. Pacureanu, C. Guilloud, Y. Yang, J. C. da Silva, J. Laurencin, F. Lefebvre-Joud, P. Cloetens, Efficient correction of wavefront inhomogeneities in x-ray holographic nanotomography by random sample displacement, Applied Physics Letters 112 (20) (2018) 203704. arXiv:https://doi.org/10.1063/1.5026462, doi:10.1063/1.5026462.
[33] M. Hubert, Durability of solid oxide cells : an experimental and modelling investigation based on synchrotron x-ray nano-tomography characterization, Thesis of Grenoble University (2017).
[34] F. Usseglio-Viretta, J. Laurencin, G. Delette, J. Villanova, P. Cloetens, D. Leguillon, Quantitative microstructure characterization of a ni–ysz bi-layer coupled with simulated electrode polarisation, Journal of Power Sources 256 (2014) 394–403. doi:https://doi.org/10.1016/j.jpowsour.2014.01.094.
[35] D. Legland, K. Kiêu, M.-F. Devaux, Computation of minkowski measures on 2d and 3d binary images, Image Analysis & Stereology 26 (2) (2011) 83–92. doi:10.5566/ias.v26.p83-92.
[36] M. B. Clennell, Tortuosity: a guide through the maze, Geological Society, London, Special Publications 122 (1) (1997) 299–344. arXiv:https://sp.lyellcollection.org/content/122/1/299.full.pdf, doi:10.1144/GSL.SP.1997.122.01.18.
[37] K. Thulasiraman, M. N. Swamy, Graphs: theory and algorithms, John Wiley & Sons, 2011.
[38] M. L. Fredman, R. E. Tarjan, Fibonacci heaps and their uses in improved network optimization algorithms (1987).
[39] A. Cecen, Tortuosity / percolation / connected path calculation for 3d structures, GitHub, retrieved January 15 (2022).
URL `https://github.com/ahmetcecen/Tortuosity-MATLAB`
[40] J. Serra, Image analysis and mathematical morphology (1982).
[41] L. Holzer, D. Wiedenmann, B. Münch, L. Keller, M. Prestat, P. Gasser, I. Robertson, B. Grobéty, The influence of constrictivity on the effective transport properties of porous layers in electrolysis and fuel cells, Journal of Materials Science 48 (7) (2013) 2934–2952. doi:10.1007/s10853-012-6968-z.
[42] B. Münch, L. Holzer, Contradicting geometrical concepts in pore size analysis attained with electron microscopy and mercury intrusion, Journal of the American Ceramic Society 91 (12) (2008) 4059–4067. arXiv:https://ceramics.onlinelibrary.wiley.com/doi/pdf/10.1111/j.1551-2916.2008.02736.x, doi:https://doi.org/10.1111/j.1551-2916.2008.02736.x.
[43] M. Neumann, O. Stenzel, F. Willot, L. Holzer, V. Schmidt, Quantifying the influence of microstructure on effective conductivity and permeability: Virtual materials testing, International Journal of Solids and Structures 184 (2020) 211–220, physics and Mechanics of Random Structures: From Morphology to Material Properties. doi:https://doi.org/10.1016/j.ijsolstr.2019.03.028.
[44] F. Monaco, E. Effori, M. Hubert, E. Siebert, G. Geneste, B. Morel, E. Djurado, D. Montinaro, J. Laurencin, Electrode kinetics of porous ni-3ysz cermet operated in fuel cell and electrolysis modes for solid oxide cell application, Electrochimica Acta 389 (2021) 138765.
[45] J. Kingman, Poisson Processes, Oxford science publications, Clarendon Press, 1993.
[46] J. Neyman, E. L. Scott, Statistical approach to problems of cosmology, Journal of the Royal Statistical Society. Series B (Methodological) 20 (1) (1958) 1–43.
[47] S. Chiu, D. Stoyan, W. Kendall, J. Mecke, Stochastic Geometry and Its Applications, Wiley Series in Probability and Statistics, Wiley, 2013.
[48] R. K. Milne, Point processes and some related processes, in: Stochastic Processes: Theory and Methods, Vol. 19 of Handbook of Statistics, Elsevier, 2001, pp. 599–641. doi:https://doi.org/10.1016/S0169-7161(01)19020-6.
[49] P. F. Felzenszwalb, D. P. Huttenlocher, Distance transforms of sampled functions, Theory of Computing 8 (19) (2012) 415–428. doi:10.4086/toc.2012.v008a019.
[50] S. Blackman, R. Popoli, Design and Analysis of Modern Tracking Systems, Artech House Publishers, 1999.
[51] X. Guo, A. Srivastava, S. Sarkar, A quotient space formulation for statistical analysis of graphical data, CoRR abs/1909.12907 (2019). arXiv:1909.12907.
[52] X. Guo, A. B. Bal, T. Needham, A. Srivastava, Statistical shape analysis of brain arterial networks (BAN), CoRR abs/2007.04793 (2020). arXiv:2007.04793.
[53] T. C. Koopmans, M. Beckmann, Assignment problems and the location of economic activities, Econometrica 25 (1) (1957) 53–76.
[54] J. T. Vogelstein, J. M. Conroy, V. Lyzinski, L. J. Podrazik, S. G. Kratzer, E. T. Harley, D. E. Fishkind, R. J. Vogelstein, C. E. Priebe, Fast approximate quadratic programming for graph matching, PLOS ONE 10 (4) (2015) 1–17. doi:10.1371/journal.pone.0121002.
[55] M. Frank, P. Wolfe, An algorithm for quadratic programming, Naval Research Logistics Quarterly 3 (1-2) (1956) 95–110.
[56] H. W. Kuhn, The Hungarian Method for the Assignment Problem, Naval Research Logistics Quarterly 2 (1–2) (1955) 83–97. doi:10.1002/nav.3800020109.
[57] A. Auger, N. Hansen, A restart cma evolution strategy with increasing population size, Proc. IEEE Congress Evolutionary Computation 2 (2005) 1769–1776. doi:10.1109/CEC.2005.1554902.
[58] A. Auger, N. Hansen, Tutorial cma-es: evolution strategies and covariance matrix adaptation (01 2012). doi:10.1145/2330784.2330919.